Available online at www.sciencedirect.com
ScienceDirect
Journal of Power Sources 166 (2007) 273–283
JOURNAL OF POWER SOURCES
www.elsevier.com/locate/jpowsour

Reserve, thin form-factor, hypochlorite-based cells for powering portable systems: Manufacture (including MEMS processes), performance and characterization

Andres M. Cardenas-Valencia [a,*], Carl J. Biver [a,b], Larry Langebrake [a]

[a] *Center for Ocean Technology, University of South Florida, 140 Seventh Ave. S., St. Petersburg, FL, United States*
[b] *Department of Chemical Engineering, University of South Florida, 4202 E. Fowler Ave. Tampa, FL, United States*

Received 29 November 2006; received in revised form 5 December 2006; accepted 7 December 2006
Available online 12 January 2007

Abstract

This work focuses on fabrication routes and performance evaluation of thin form-factors, reserve cells, as a powering alternative for expendable and/or remotely operated systems. The catalytic decomposition of sodium hypochlorite solutions is revisited herein with two cost-effective anodes: zinc and aluminum. Aluminum, even though the most expensive of the utilized anodes, constituted cells with double the energy content (up to 55 Wh kg^{-1}) than those fabricated with zinc. Even though the hypochlorite concentration in the solution limits the cells' operational life, attractive performances (1.0 V with a current of 10 mA) for the manufactured cells are obtained. It is shown that micro fabrication processes, allowing for close electrodes interspacing, provided high faradic and columbic efficiencies of up to 70 and 100%, respectively. Obtained specific energies (50–120 Wh kg^{-1}) are in the same order of magnitude than batteries currently used for powering deployable systems. Experimental results show that a simple model that linearly relates over potentials and the electrical load, adequately describe all the cell designs. A mathematical model based on a kinetic–mechanistic scheme that relates the current output as a function of time agrees fairly well with results obtained activating cells with various concentrations of NaOCl solutions.

Keywords: Hypochlorite; Catalytic metals; Zinc; Aluminum; Batteries; Cells

1. Introduction

Traditionally, batteries are classified into three groups [1–3]: (1) primary or expendable, (2) rechargeable or secondary, and (3) reserve systems, which remain inactive until the cell circuit is closed. Primary and rechargeable batteries are widely utilized in diverse applications. For instance, to date, disposable alkaline batteries dominate the market of common household electronics (clocks and toys, for instance) [1–3]. House and mobile phones as well as specialized deployable sensors for environmental, oceanographic, and even military surveillance commonly use rechargeable batteries. Lead–acid batteries, an inexpensive and reliable system [4–7], are being replaced by nickel–cadmium, and metal hydride cells, either as emergency [7–9] or main power supplies [10]. Newer transducers and exploratory vehicles have incorporated lithium-based cells [11,12], a system with high specific energy [7,13,14]. Self-discharging characteristics, and safety (including the manufacture of lithium cells), are well documented concerns for primary and rechargeable cells [1,2,13,15]. As for reserve batteries, even with their distinct advantageous features (such as slight degradation over time and providing large current discharge capability), their use has been mainly restricted to specific applications. In this paper, the construction and evaluation of various types of safe, reserve cells for powering remotely operated systems are investigated. Table 1 summarizes some of the most commonly used battery systems.

1.1. Micro electromechanical systems, MEMS and batteries

The well-known advantages of micron-scale transducers have motivated the development of many portable, in situ MEMS-based and "lab-on-a-chip" sensors. Using standard manufacturing processes typical of the integrated circuit industry,

* Corresponding author. Tel.: +1 727 5531198; fax: +1 727 5533967.
E-mail address: cardenas@marine.usf.edu (A.M. Cardenas-Valencia).

0378-7753/$ – see front matter © 2007 Elsevier B.V. All rights reserved.
doi:10.1016/j.jpowsour.2006.12.070

Table 1
Performance characteristics of reserve batteries (1–5) and several commercially available cells (7–11)

System name	Anode	Cathode	Electrolyte	Cell voltage	Energy content		Applications, and production status
					$Wh\,kg^{-1}$	$Wh\,L^{-1}$	
Reserve battery systems							
1. Water activated	Mg, Zn	MnO_2	H_2O, seawater solutions	1.5–1.6	90–150	50–200	Limited marine use and rescue; emergency lights
2. Metal air	Zn, Mg, Al	Air or oxygen	Seawater or OH^- solution	1.0–1.4	200–400	650–1000	Use in consumer applications as button cells
3. Lithium–H_2O	Li	$H_2O_{2(aq)}$, O_2	H_2O, LiOH	2.2	160	135	In development
4. Zinc–silver oxide	Zn	AgO, Ag_2O	KOH	1.6	20–60	100–160	Missile and torpedo applications
5. Organic Li	Li	V_2O_5, SO_2, $SOCl_2$	Organic $SOCl_2$	3.0–3.5	50–150	100–300	Mine fuzing, missiles
6. Thermal batteries	Ca, Mg, Li	$CaCrO_4$, V_2O_5, FeS_2	LiCl/KCl	1.6–2.7	10–40	30–100	Military production, rockets, projectiles.

System name	Anode	Cathode	Cell voltage	Energy content		Comments
				$Wh\,kg^{-1}$	$Wh\,L^{-1}$	
Rechargeable battery systems (unless indicated)						
7. Alkaline–primary	Zn	MnO_2	1.6	145	400	Have dominated the market since the 1960's
8. Lead–acid	Pb	PbO_2	2.1	35	70	A commercial success for the last 40 years. Use include cars and customer appliances
9. Nickel–cadmium	Cd	Ni oxide	1.4	35	100	In production. Used in inhalambric phones, and consumer electronics
10. Ni–metal hydride	MH	Ni oxide	1.4	75	240	Currently, they displace Ni–Cd batteries
11. Lithium-ion	Li_xC_6	$Li_{(1-x)}CoO_2$	4.1	150	400	Rapidly increasing the type of applications

The table shows that activation in reserve cells can also be achieved (additionally to reagent addition) by melting a salt hosted within the cell.

lowers fabrication costs, allowing for the development of single-use, expendable devices [16]. This new generation of devices requires powering systems with smaller sizes (or with specific form-factors), that have been labeled power-MEMS. Fuel cells and micro batteries are examples of electrochemical-based power MEMS [17–29]. Interestingly, many of the micro batteries are of the reserve type since heir activation relies on the injection of a liquid electrolyte [22–29]. In fact, a variety of micro fluidics activation schemes have been described in the literature [23,25]. Micro fabrication processes are a natural choice for building mini-batteries, since structures with very small interspacing (in these case the battery electrodes) are readily manufactured. In this work cells constructed using simple material layering are compared others fabricated via MEMS processing. The performance of the cells is experimentally investigated and simple mathematical models are evaluated as possible characterizers.

2. Rationale on the utilized hypochlorite chemistry and theoretical background

The physicochemical characteristics of materials that participate in a galvanic cell dictate the attainable specific energy (energy per unit weight) as well as its theoretical energy density (energetic content per unit volume). Table 2 summarizes common metallic anodes used in galvanic cells, and shows that lithium has the highest specific energy, while the highest energy density corresponds to aluminum, explaining the reports that continue to appear expounding the merits of this material [29–37]. Currently zinc and aluminum, after lithium, as shown in Table 2 are the most cost-effective energetic anodes [38], that have been used to fabricate micro cells. These are activated with alkaline solutions and peroxide or air cathodes, providing high energetic densities [22,23,28,29]. Zinc, as an anode, suffers from its high atomic weight and that explains why oxygen from air has been coupled with it to produce batteries with high energy contents. Metal-air cells of this nature can not be used in underwater marine applications. Competing reactions, some of which release gas bubbles that interfere with the electrode processes, reduce the operational lives of the aluminum-anode cells. Flushing electrolyte through the cell dislodges the bubbles [32,34], and balancing of cathode reactions either by electrode area variation or via solid peroxides, whose dissolution controls hydroxide-ions levels [33], have been proposed to improve the performance of Al-anode cells. However, a more complex packaging is needed to implement these improvements. Ten years ago, Brenner reported aluminum and magnesium anodes cells activated with chlorite and hypochlorite solutions [35]. The same anodes, reported by Medeiros et al., in electrolyte flow cells systems provided impressive currents when hydroxide ions are added to the electrolyte [36,37]. In this present work, the decomposition of sodium hypochlorite ($NaClO_{(aq)}$) is coupled, in a first set of experiments, with zinc and aluminum. Table 3 shows the electrochemical equivalents of solutions of this cathode electrolyte. Other cathode materials are included in the table for comparison purposes. Oxygen has been coupled to both zinc and aluminum in the past, while hydrogen peroxide is a cathode that has been used in the development

Table 2
Physicochemical properties of various common anode materials, and theoretical maximum energetic properties per unit mass, volume and cost

Metal	Valence (or oxidation state change)	Atomic weight ($g\,mol^{-1}$)	Density ($g\,cm^{-3}$)	Electrochemical equivalents and energetic content			Stored energy per cost of anode[a]	
				Specific current ($Ah\,g^{-1}$)	Specific energy ($Wh\,g^{-1}$)	Energy density ($Wh\,cm^{-3}$)	$Ah\,US\$^{-1}$	$Wh\,US\$^{-1}$
Li	1	6.9	0.54	3.86	11.7	6.32	3.57[b]	10.83[b]
Mg	2	24.3	1.74	2.20	5.23	9.10	0.04	0.08
Al	3	26.9	2.69	2.98	4.96	13.35	0.57	0.94
Zn	2	654	7.14	0.82	0.62	4.45	2.26	1.71
Fe	2	55.8	7.85	0.96	0.42	3.31	0.07	0.36
Pb	2	207.2	11.34	0.26	0.03	0.38	0.05	0.01

Energy content calculated using the assumed the half-reaction reversible potential at standard conditions.
[a] Calculated using the monetary value (2006 taken from Alfa Aesar Catalog [37]) of the metal with purities of at least 99.98% purity in foil form with a thickness of 0.25 mm except lithium (1.5 mm).
[b] Includes price of safe packaging under argon.

of aluminum-anode power sources. Table 2 shows that similar reversible potential values at standard conditions are available with $NaOCl_{(aq)}$ and $H_2O_{2(aq)}$. It is clear that owing to its smaller molecular size, hydrogen peroxide theoretically provides higher capacities than hypochlorite ions. However, it is also known that this cathode presents reactions paths that do not correspond to the energy producing reaction. The metal anode that constitutes the most advantageous cell with hypochlorite is to be incorporated to various cell designs in other fabrication routes of cells that are also characterized herein. The chemistry of the cell system can be described as follows. The oxidation of the metals, M, losing Z electron-moles, $\bar{e}$ is the generic anode reaction,

$$M \rightarrow M_{(aq)}{}^{Z+} + Z\bar{e} \quad (1)$$

The standard oxidation potentials are 1.7 V for aluminum ($Z=3$), and 0.7 V for zinc ($Z=2$). The cathode half-reaction and its standard oxidation potential, E^o are

$$OCl_{(aq)}{}^{-} + H_2O + 2\bar{e} \leftrightarrow 2OH_{(aq)}{}^{-} + Cl_{(aq)}{}^{-}, \quad E^o = 0.9\,V \quad (2)$$

The most likely overall reactions for aluminum and zinc are then:

$$2Al + 3NaOCl + 3H_2O \leftrightarrow 3Na^+ + 3Cl^- + 2Al(OH)_3 \quad (3)$$

$$Zn + 2NaOCl + 2H_2O \leftrightarrow 2Na^+ + 2Cl^- + Zn(OH)_2 \quad (4)$$

Fig. 1 where a depiction of the cell is also illustrated, presents a mechanistic route for the subsequent reaction of the hydroxide ions with the anode, once they have been generated in the catalyzed NaOCl decomposition reaction (Eq. (2)). The proposed route suggests that the alkalinity of the solution will be kept at low levels, and minimal corrosion reaction of aluminum is expected. Given this contention, and since no other decomposition of reagents takes place (as in cells with peroxide solutions [33]), the galvanic couple will not produce gas bubbles, an especially important feature when the electrodes are closely spaced. Another advantage of the relatively simple chemistry described in Eqs. (1)–(4), is that the power output should be constant and that basic electrochemistry and simple chemical kinetics concepts can be used to model the chemical processes. Appendices A and B describe the derivation of possible characterizing models for use in cell design. First, it is shown that the cell potential, V_{load}, the electrodes separation to area ratio, d/A, the open circuit

Table 3
Characteristics of common oxidizers utilized as cathode materials

Cathode material	Desired reaction and comments	E^o (V)[a]	Aqueous concentration (wt%)	Theoretical values[b]	
				Current content ($Ah\,g^{-1}$)	Energy content ($Wh\,g^{-1}$)
Oxygen	$O_{2(g)} + H_2O + 4\bar{e} \rightarrow 4OH_{(aq)}{}^{-}$, in alkaline solution	+0.41	Dictated by the oxygen solubility	2.14[c]	0.88
Hydrogen peroxide	$H_2O_{(aq)} + OH_{(aq)}{}^{-} + 2\bar{e} \rightarrow 3OH_{(aq)}{}^{-}$	+0.88	3	0.05	0.04
			5	0.08	0.15
			10	0.07	0.13
Hypochlorite ion	$ClO_{(aq)}{}^{-} + H_2O_{(l)} + 2\bar{e} \leftrightarrow Cl_{(aq)}{}^{-} + 2OH_{(aq)}{}^{-}$	+0.90	3	0.02	0.01
			5	0.03	0.05
			10	0.02	0.05

[a] Values taken from Lange's Handbook of Chemistry, 11th ed.
[b] Values have been calculated assuming that the standard potential (reversible work) takes place regardless of the chemical concentration.
[c] The water molecule has been included in this calculation.

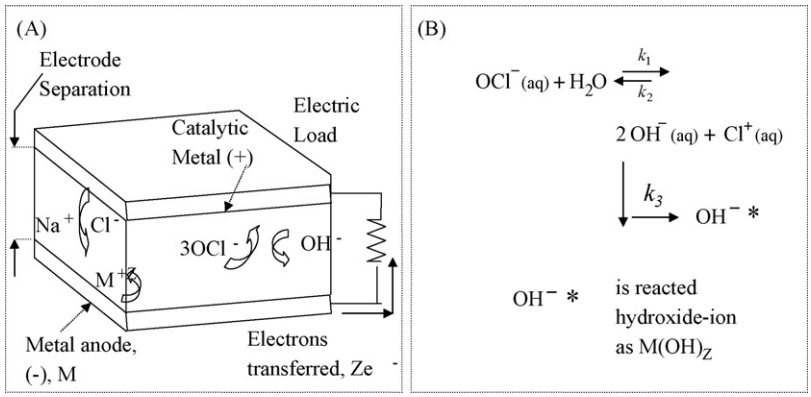

Fig. 1. (A) Schematic of an aluminum-anode hypochlorite ion-catalytic metal cell. (B) Proposed two-step mechanistic route for the production of $OH_{(aq)}^-$ and its reaction with the metallic anodes.

voltage, V_{oc}, and a given load, R_{load}, are related by an expression of following form:

$$V_{load} = C \ln\left(\frac{C_1 d}{A}\right) + C_2 \ln(R_{load}) \quad (5)$$

Second, if a chemical reaction sequence such as that shown in Fig. 1(B) takes place, the current profile i normalized to the initial current i_o, as a function of time is given by Eq. (6). The relationships between groups of physical constants and the coefficients of Eqs. (5) and (6) are derived in Appendices A and B.

$$\frac{i}{i_o} = C_3\, e^{C_4 t} + C_5\, e^{C_6 t} \quad (6)$$

3. Cell fabrication

The fabrication of two cell types is schematically shown in Fig. 2, where pictures of the finished cells are also illustrated. Fig. 2(A1) shows a rigid cell that has been fabricated by layering a silicon wafer with a sputtered platinum electrode, with a frame machined from polysulfone (0.03 in.-thick acquired from Kmac plastics, Wyoming, MI), a high-temperature plastic material, and the anode material (Al or Zn). Each layer was glued using a polyurethane adhesive (Gorilla glue®, Cincinnati, OH). These macro "stack-ups" were used to compare the performance between aluminum and zinc cells, before proceeding with the additional micro fabrication steps of the MEMS process flow

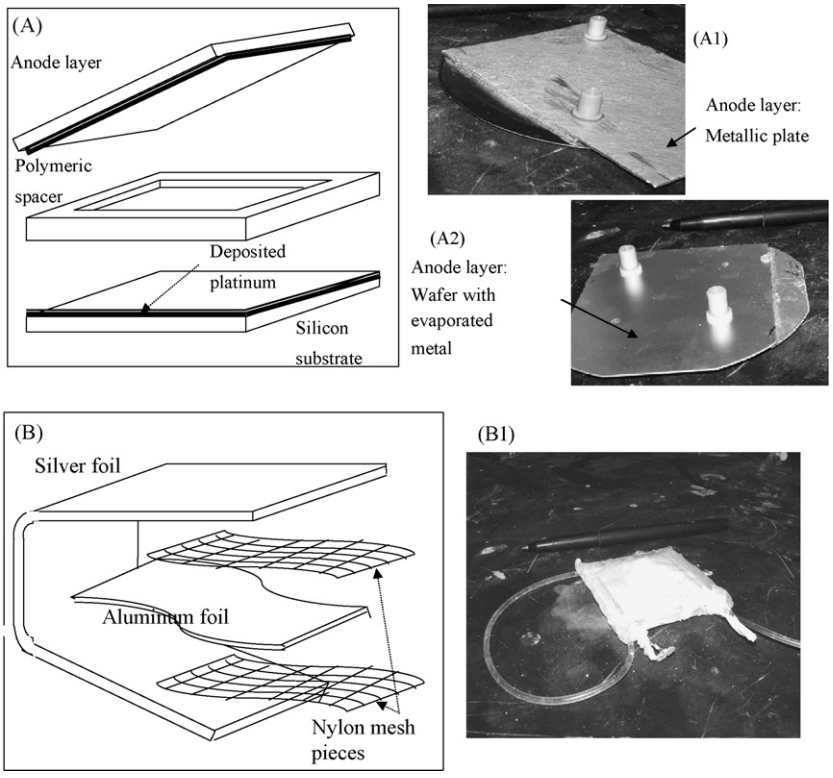

Fig. 2. Isometric views (not to scale) of the constitutive layers and basic configuration of the fabricated cells (A) Rigid cells (B) Flexible cell. Pictures of finished devices (A1) Using a metal plate as anode (A2) Using 2 silicon wafers onto which the electrodes have been deposited (B1) Flexible cell.

Table 4
Description of materials used to fabricate the cell designs, and some of their resulting characteristics

Cell type (Fig. 3)	Cell ID	Materials used for construction and some of their general characteristics	Electrodes separation	Cell electrode areas	Hosted electrolyte
A	A1	Anode: 25 mm-thick aluminum and zinc plates (Alfa Aesar) Separator: machined polysulfone (K-Mac Plastics) plastic separator Cathode: sputtered platinum on silicon wafer	700 μm	20 cm^2	1 mL
	A2	Anode: evaporated aluminum on glass wafers Separator: patterned BCB 4026 cyclotene resin Cathode: sputtered platinum on silicon wafer	18 μm	10 cm^2	18 μL
B	B1	Anode: aluminum foil (Alfa aesar) Separator: poly-ester mesh Cathode: silver foil Encased in transparent polypropylene bag	500 um	50 cm^2	9 mL

(Section 3.1), that lead to the cell type labeled as A2. The flexible cell version (Fig. 2(B)) was fabricated using a flexible poly(ester) mesh as a separator to avoid short-circuiting of the electrodes. In the case of cells A1 and A2, the electrodes are separated by a rigid spacer and are which prevents short-circuiting. In the case of the flexible cells, both sides of the aluminum electrode were used. The electrodes were fabricated using commercially available high purity thin foils (Alfa Aesar) of silver and aluminum, allowing for this design to keep its flexible characteristics. In this case an electrode separating layer between electrodes is included. Table 4 presents the layering of materials used in the cell design fabrication, and some of the cells' resulting characteristics. Either fluidic nanoports or flexible Tygon hoses (Upchurch Scientific) were attached to the cells, for injection of electrolyte. A 10% solution of sodium hypochlorite (Chlorinazor from Aquachem) was used as the electrolyte stock solution. This solution was used to test the three fabricated cells under various resistive loads, to study the cells' current and voltage characteristics. The NaOCl solution, either diluted with DI water, or concentrated by evaporation (at 70 °C), produced NaOCl solutions of various concentrations. Potassium chloride salt (obtained from Fisher Scientific) was added to form a 3.0 M solution of this reagent. The addition of KCl (or NaCl) to the electrolyte solution increases the solution conductivity (reducing the cell's internal resistance), and in turn provides a higher cell potential [29]. The anode metal loss by cells' reactions was obtained by weight difference using a precision analytical balance (Model PI 225D, Denver instruments).

3.1. MEMS fabrication procedure

Benzocyclyobutene (BCB Dow Chemical Co. resin 4026), a photo-patternable material, is used here with a two-fold objective: as the adhesive material between wafers and to form the cell cavity (Fig. 2(A2)). Manufacturer recommendations [39] with slight modifications were followed for the BCB patterning procedure but it was tuned to obtain satisfactory deposition, patterning and bonding. The wafers surfaces are cleaned by acetone and methanol dispensing while rotating at 2500 rpm for 30 s (Laurell Corp. WS-400B-6NPP/Lite spinner). Fig. 3 shows schematically the MEMS-based processing steps utilized to fabricate the type A2 cells (in Table 4). The platinum sputtering onto a titanium interface adhesive layer, and aluminum wafer (steps A1–A3 and B1–B5 in Fig. 3) processing conditions can be found elsewhere [29]. An adhesion promoter (AP3000) is applied while the silicon wafer is stationary on the spinner and spread into a thin layer (30 s). The wafers are then "spun-dry" at 3000 rpm for 10–20 s. The wafers are then hot-plate baked at 125 °C for 30 s. The BCB is applied on the wafer, spread by rotating the spinner at 700 rpm for approximately 10 s. A rotation at 1200 rpm for 30 s resulted in a BCB thickness of 18 ± 3 μm. A thickness of ±4 μm was calculated as twice the standard deviation of measurements from at least five replications. After BCB-resin is applied, a 1 min hot-plate (Delta 20T2 3LE) bake at 85 °C was performed, partially hardening the resin. Cyclotene is a photo-negative resin, so masks drawn accordingly were prepared (Coventor software) and printed on transparency millard paper at Precision Images Inc. (Largo FL). Processing conditions to attain other BCB thicknesses, the masking pattern that allowed for wafer to wafer bonding, and other bonding conditions are subject of a paper in preparation [40]. The recommended exposure dose of 60 mJ cm^{-2} μm^{-1} [39] was used in an EV-620 photolithoraphy system. A 10 min soft-bake (75 °C) during 10 min (Ultraclean 100 In-Line Instruments) greatly enhanced the cyclotene resin development. Puddle development was found to be more reliable than immersion development. Wafers were placed on spinner, and while spinning (700 rpm), DS2100 developer was added drop by drop for 10 s, followed by a spin-drying at 3000 rpm during 30 s. This procedure is repeated three times. Wafers are then placed for 1 min in a plasma etcher (M4L Tepla) using a gas mixture of 80:20 O_2:CF4, to etch away remaining BCB-polymer.

4. Results and discussion

4.1. Comparison of results using zinc and aluminum anodes

Fig. 4 shows the potential as a function of time obtained from type A1 cells fabricated either with zinc or aluminum plates serving as anodes. Fig. 4(B) shows the time-weighted average

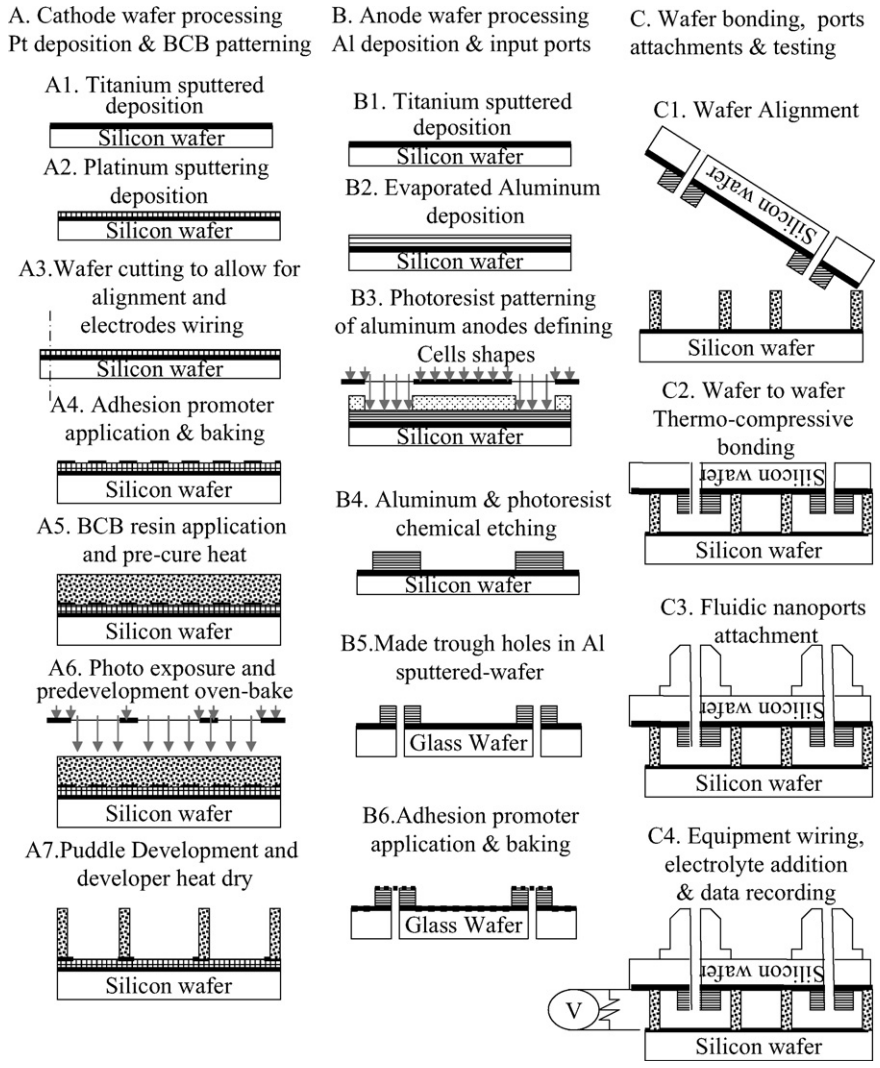

Fig. 3. Schematic of micro fabrication steps for aluminum-anode galvanic cells with micron separations in between the electrodes.

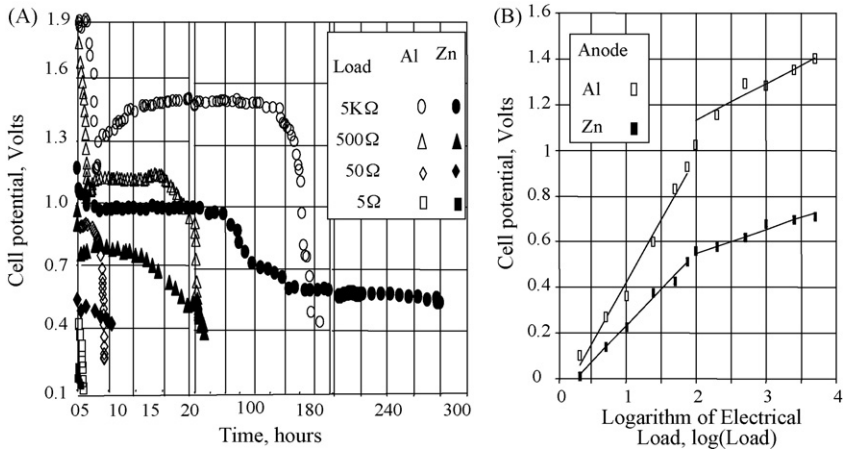

Fig. 4. Performance comparison between flat type A1 cells with different anodes. (A) Selected cell potential vs. time curves, while cells at connected to different loads. (B) Cell potential vs. logarithm of the electrical impedance load.

Table 5
Charge and energetic capacities of the fabricated A1-type (Fig. 3) cells obtained at various loads

Anode	Used load (Ω)	Overall charge and energy densities and efficiency with respect to the $ClO_{(aq)}^-$ ion		Charge and energy data per unit (weight or value) of anode material			
		Charge, Ah kg^{-1} (Columbic efficiency)	Energy, Wh kg^{-1} (Faradic efficiency)	Charge delivered		Energy delivered	
				Ah g^{-1} material	Ah US^{-1} value	Wh g^{-1} material	Wh US^{-1} value
Al	2	20.9 (30.3%)	2.09 (1.16%)	1.15	0.21	0.12	0.02
	25	39.4 (57.0%)	23.8 (13.3%)	2.18	0.42	1.32	0.25
	75	49.3 (71.4%)	45.9 (25.5%)	3.91	0.74	3.64	0.70
	200	45.6 (66.0%)	50.4 (28.1%)	5.28	1.01	6.36	1.21
	2.5k	45.0 (65.1%)	54.9 (30.6%)	5.74	1.10	7.02	1.34
Zn	2	7.58 (22.4%)	0.15 (0.26%)	0.97	2.68	0.048	0.13
	25	35.0 (>100%)	13.4 (23.2%)	1.15	3.19	0.44	1.22
	75	34.9 (>100%)	18.3 (31.6%)	1.35	3.73	0.70	2.05
	200	29.8 (>87.8%)	18.8 (32.6%)	1.30	3.59	0.70	1.90
	2.5k	27.7 (>81.8%)	21.5 (37.3%)	0.89	2.46	0.71	1.91

The cells volume is 1.0 mL.

voltage output as a function of the logarithm of all of the electrical loads used in the testing of the fabricated cells. The data markers in Fig. 4(B) represent experimental data, and the lines are the best straight-line fit calculated by least-squares regression. Two straight lines are required to represent each data set. Such straight lines, each representing ionic transfer dominance at each of the cells' electrodes, are an adequate representation for the experimental data (Eq. (5)), and characterize the fabricated cells. Table 5 summarizes the capacity of the cells as well as the charge and energy efficiencies that have been calculated by integrating the instantaneous current, $I(t)$, and power, $P(t)$, with respect to time, t, data according to the following formulas:

$$\text{Columbic efficiency}\,(\%) = 100 \int I(t)\,\mathrm{d}t, \quad \text{Theoretical delivered charge} \tag{7}$$

$$\text{Faradic efficiency}\,(\%) = 100 \int P(t)\,\mathrm{d}t, \quad \text{Theoretical delivered energy} \tag{8}$$

The theoretical delivered energy was calculated using the E^o and the stoichiometry of the chemical reactions, represented by Eqs. (3) and (4). These calculations assume that the 10% hypochlorite solution is completely utilized. Table 5 also shows both the current and energy per unit weight and per commercial value (US$ wt^{-1}) of the anodes. It is clear that even though, the higher price of aluminum when compared to that of zinc (a 99.99% pure piece is 15 times more expensive) causes the price of current and energy generated by a zinc cell to be more cost-effective than that of an aluminum cell, the aluminum cells produce considerably higher potentials in a $ClO_{(aq)}$ electrochemical cell. The aluminum cells provide (even if the efficiency is smaller than of zinc) almost three times the specific energy and double the specific current in a cell of the same size (1 mm × 4.5 cm × 4.5 cm). The energy provided per gram of aluminum is about 20 kJ g^{-1}, a higher value than those obtained in aluminum-anode cells with $H_2O_{2(aq)}$–alkaline solutions [41]. This fact evidences that even though $NaOCl_{(aq)}$ electrolyte possesses an intrinsically lower current and energy content when compared to hydrogen peroxide (Table 3), its utilization take place following the most favorable electrochemical route in a more effective manner.

4.2. Cell capacity and comparison of cell performance as function of the current load

Voltage profiles as function of time are shown in Figs. 5 and 6, for the cells labeled as A1 and A2, respectively. The marked data points are shown at arbitrary time intervals, and were calculated as an average from at least four replicated runs for each resistive load. The errors bars represent the span of measured voltages. Notice that the variability of the cell voltage output, as indicated by the error bars generally becomes larger as the delivered power increases, a fact that is probably due to complex ionic transfer limitations. It is interesting to note that all the potential versus time curve presented show an initial period that exhibits a high potential output. For instance, Figs. 5 and 6 shows a potential close to 1.75 V during the first 2 h and 5 min, respectively, imme-

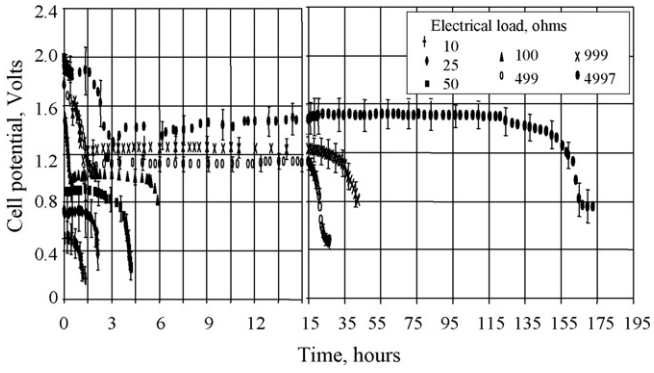

Fig. 5. Cell potential as function of time under selected loads for a 20 cm^2-cell with an electrode separation of 700 μm (cell type A1 in Table 3). The calculation of shown error bars are described in the text.

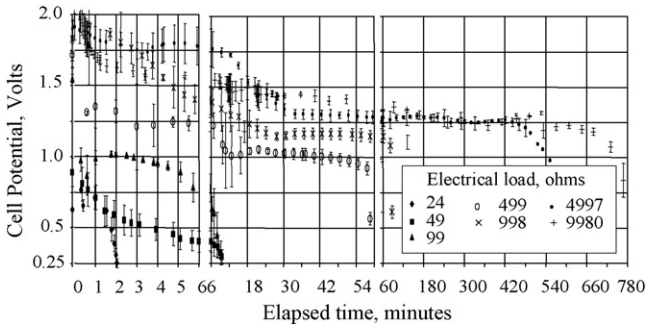

Fig. 6. Cell potential as function of time under selected loads for a 10 cm^2-cell with an electrode separation of 20 μm (cell labeled as A2 in Table 3). Depicted error bars have been obtained as explained in the text.

diately after the electrolyte is injected. This is very likely due to the initial presence of hydroxide ions in the hypochlorite solution that is required to stabilize such a solution [42]. This high potential output is probably responsible for obtaining columbic efficiencies in excess to 100% (as shown in Table 4). After that initial high-potential phase, the potential stabilizes to a value that is maintained almost as a constant value until the cell eventually dies. The higher electrolyte conductivity in this set of experiments, due to the presence of the ionized potassium chloride salt, did indeed increase the potential of the cell. The average voltage obtained with nominal loads of 50 and 5000 Ω are shown to be 0.1 V higher (in the curve section where the potential has stabilized, which constitute the majority of the operational time of the cell), when the salt is present (Fig. 5) than when it is not (Fig. 4(A)).

As one would expect, the dimensions of the active electrodes greatly affect their energy and current capacity. Figs. 5 and 6 clearly show that, as expected, the life of the cells varies considerable with the amount of electrolyte (minutes versus hours). The flexible cell (labeled B-type design in Table 4) was built with a higher *d*/*A*-ratio (in Eq. (5)) and to contain 9 mL of electrolyte. Fig. 7 shows the potential obtained as a function of the logarithm of the resistive load. Experimental data (as data markers) are co-plotted with the regressed model that characterizes each fabricated cell. It was found that for every tested case (including zinc-anode A1-type cells, shown in Fig. 4), that even though the electrodes configuration and the overall volume affect the cell capacity, a linear relationship between the logarithmic load and

Table 6
Linear parameters that characterize the potential vs. ln(load) regressed from experimental data for the three fabricated cells

Cell type (Fig. 3)	Cell ID	Slope	Intercept	Correlation coefficient
A	A1	0.2444	−0.3294	0.9824
		0.0589	0.7322	0.9722
	A2	0.2072	0.0596	0.9967
		0.1236	0.4313	0.9929
B	B	0.0966	0.4537	0.9938
		0.0967	0.5840	0.9898

the potential output is an adequate representation in any of the cell designs described herein (Eq. (5)). This is supported by the correlation coefficient, which is very close to unity for all the presented cases. Regressed slopes and intercepts of such linear relations (in Fig. 7) are shown in Table 6. A comparison between the calculated energetic density and power volume densities per unit of available electrode area is presented in Fig. 8. The volume of injected electrolyte is assumed to be the cell volume only since the volume of the aluminum and cathode electrodes are very small, and can be considered negligible, when compared to that of the electrolyte. As expected, Ragone-type behavior is observed, i.e. highest energy densities are obtained when smaller power densities are delivered. Table 7 shows performance characteristics of the cells, evidencing the strong influence of the electrode separation and the area of the electrodes (*d*/*A*, in Eq. (5)) on the cell performance. MEMS-based cells provided the highest energy densities (of 127 Wh L^{-1}).

An easily stackable cell design was fabricated (similar to the A1-type cells but using the cathode collector of the cells labeled as B), and with electrode areas of 15 cm^2 and an interspace separation of 0.1 cm. Since the *d*/*A*-value (in cm^{-1}) falls within the *d*/*A* ratios of the A2 cells, and the A1-type design, $1.7 \times 10^{-4} < 6.7 \times 10^{-4} < 3.5 \times 10^{-3}$, a fair assumption is that a potential of 1 V would be obtained with such a cell when connected to a 100 Ω load. Also, if a Faraday-efficiency of 23% is attainable (as could be deduced from the data in Table 7) when subjecting a cell to a 100 Ω load, the expected life of the cell would be around 5.5 h. Fig. 9 shows the potential obtained from a battery of four cells in series, and a picture of this battery. The

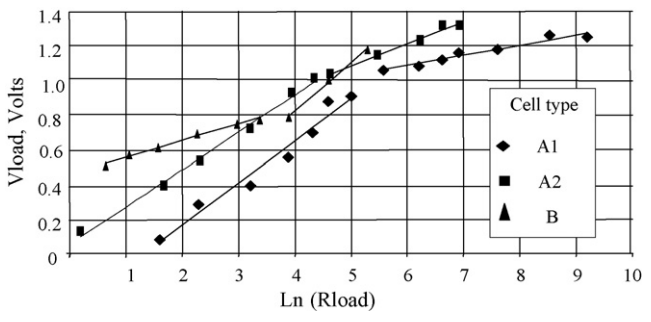

Fig. 7. Comparison of the voltage under load as a function of the natural logarithm of the utilized resistive load.

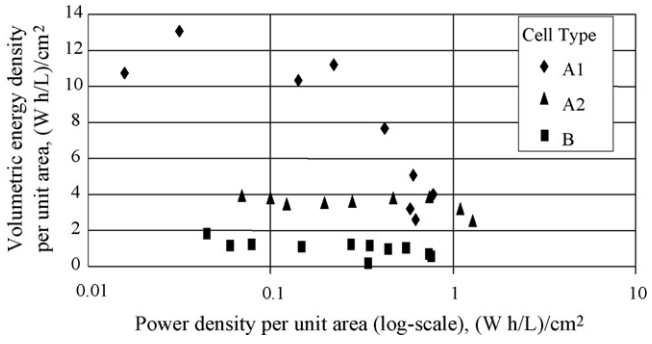

Fig. 8. Ragone plots (energy density vs. power density) for the three fabricated cell designs.

Table 7
Capacities and efficiencies of the fabricated cells under various loads

Cell type/load (Ω)	Average potential (V)	Operational time (h, unless indicated)	Gravimetric specific cell capacities		Efficiency	
			Current (Ah kg^{-1})	Energy (Wh kg^{-1})	Columbic (%)	Faradic (%)
A1/10	0.40	1.4	48.0	19.2	4.2	9.5
A1/100	0.97	5.8	43.8	42.5	62.0	23.1
A1/5k	1.42	155	34.3	48.7	48.5	26.5
A2/100	0.93	6.6 min	46.9	43.6	66.3	23.7
A2/5k	1.4	7.5	90.9	127.3	>100	69.2
B/100	1.1	45	42.8	46.1	57.2	23.0

The cells were activated with 10% hypochlorite solutions.

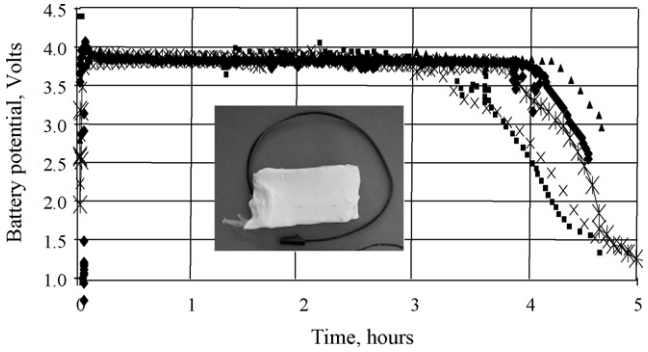

Fig. 9. Battery potential as function of time under a load of 10 Ω. Picture shows the fabricated battery that stacks 4 cells with and area 3 cm × 15 cm.

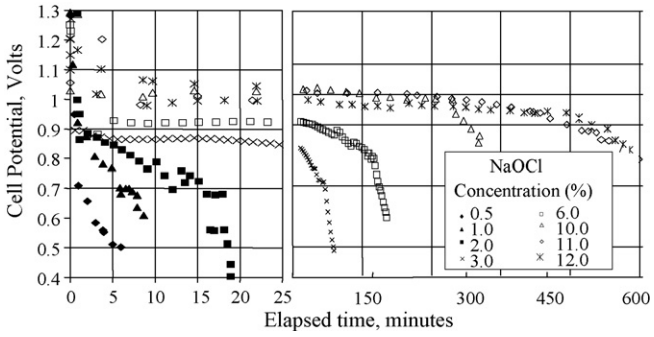

Fig. 10. Cell potential as function of time under a load of 100 Ω obtained. From A1-type cells that have been activated with solutions of NaOCl of various concentrations.

average battery life while providing 10 mA was 4.8 h, a value 13%-off the value inferred above.

4.3. Experimental results with various $OCl_{(aq)}^-$ concentrations and basic kinetic modeling

Stoichiometry suggests that higher concentrations of hypochlorite ion in the electrolyte would result in increased operational life for the cells. Additionally, the Nerst equation (basic thermodynamics) suggests that higher potentials should be possible with increased concentrations. For these reasons, more concentrated solutions in hypochlorite ions were used to activate cells of the A1-type in which the Faradic efficiency was low even for low current drains (between 20 and 30%). Cell potential versus time curves from cells activated with solutions of various NaOCl concentrations in Fig. 10. Table 8 shows the magnitude of the improvement in the performance characteristics of the cells when using higher concentrations of sodium hypochlorite solutions. Additionally, the table shows regressed parameters obtained using a numerical non-linear Marquardt optimization routine that fitted the experimental data of the current (normalized to the initial current), shown as markers in Fig. 11, with an expression like Eq. (6). These parameters were used to calculate the continuous lines presented evidencing the adequacy of Eq. (6) to represent the current delivery as a function of time.

Table 8
Performance characteristics of the A1-type cell activated with hypochlorite solution of various concentrations while subjected to a 100 Ω load impedance

NaOCl concentration (%)	Average potential (V)	Operational time (h)	Specific cell capacities and (efficiencies)		Parameters (Eq. (6))				RMSE × 10^2
			Current, Ah kg^{-1} (Columbic)	Energy, Wh kg^{-1} (Faradic)	C_3	C_4	C_5	C_6	
0.5	0.45	0.10	0.39 (10.7%)	0.17 (1.85%)	0.65	5.4×10^{-2}	0.63	1.92	2.56
1	0.70	0.15	0.90 (12.5%)	0.63 (3.4%)	0.74	4.2×10^{-2}	0.31	2.2	1.46
2	0.80	0.30	2.02 (14.1%)	1.62 (4.3%)	0.71	2.1×10^{-2}	0.41	1.54	5.55
3	0.87	1.10	8.12 (37.6%)	7.06 (12.6%)	0.72	4.4×10^{-3}	0.23	1.11	4.71
6	0.93	1.0	15.2 (35.4%)	14.1 (12.7%)	0.73	1.7×10^{-3}	0.27	0.42	3.88
10	0.97	5.8	43.8 (62.0%)	42.5 (23.1%)	0.80	3.0×10^{-4}	0.13	0.15	4.57
11	1.01	9.2	71.7 (92.4%)	72.4 (35.9%)	0.80	3.6×10^{-4}	0.08	0.25	3.76
12	1.03	10.4	81.9 (96.9%)	84.3 (38.4%)	0.82	2.3×10^{-4}	0.18	0.68	0.53

The last four columns show the kinetic characterization of the current drawn profile as dictated by Eq. (6).

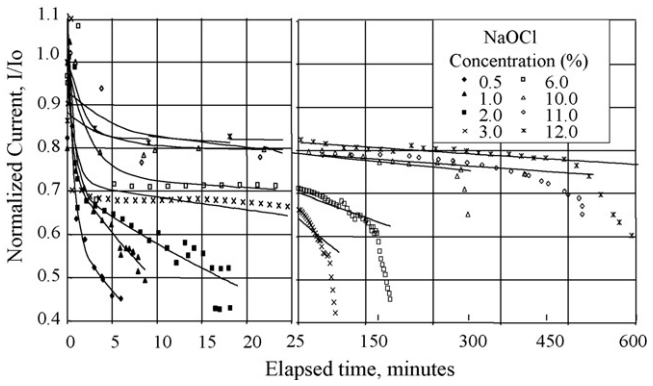

Fig. 11. Normalized current as a function of time. Constant load testing (100 Ω). Cells activated with NaOCl of different concentrations.

5. Conclusions

Various cell designs that provide good energetic densities and specific powers relative to their volume, have been constructed and tested. Electrochemical modeling suggests that the use of large electrode areas and very small separations between them are desirable considerations in the design of cells, producing higher output potentials and lower internal resistance. The experimental results show that a stable potential is obtained from the cells due to the relatively simple (in the sense that no many reactions paths take place) chemistry, that has been described. Experimental results show, that in fact, the MEMS fabricated cells provided the highest energetic densities, but their operational times were limited by the $NaOCl_{(aq)}$ content. The preliminary dynamic modeling shows that it can adequately represent experimental data, but finding further relations of the kinetic constants with the regressed parameters C_3–C_6 is still to be elucidated.

The major disadvantage of the cells lies within the fact that the hypochlorite solution could lose strength over time [35]. However, it is well-known that the solutions can be stabilized via addition of buffers. In addition, the low price of solutions of this salt makes it still an attractive alternative to be used to activate cells. Some novel applications that the fabricated cells reported herein can compete for, are based on the fact that they use a liquid electrolyte for activation. Work in progress includes the automation of electrolyte feed, by various low-energy consumption methods, for batch or continuous flow delivery [43]. If the cells are operated in this manner, then they can be used to power unattended sensors or other systems. A cell (or a number of them) could then be activated on-demand, or as the "power budget" of the system requires.

The cells may be pre-filled with liquid electrolyte before they are to be deployed in the ocean, which may eliminate the need for liquid pumping systems, in specific applications. The filling with an aqueous solution can potentially eliminate the need for a thick pressure housing of the cells. In this regard, further studies on the effects of ocean depth pressure on the physical integrity and performance of cells with electrolyte fill system requirements, are necessary and continuing. Additionally, the fact that these cells may be fabricated with thin form-factor geometry makes them capable of conforming to the body surface of a sensor or a system, facilitating the efficient utilization of space, which is critical, in mobile platforms such as AUV or ROV's.

Acknowledgements

Distribution Statement 'A'. Approved for Public Release-Distribution Unlimited. The authors acknowledge the financial support provided to the University of South Florida through grant no. DASG60-00-C-0089 that permitted the work presented herein. Mr. Dlutowski is gratefully acknowledged for processing and bonding the wafers on which metals were deposited. Dr. John Bumgarner and Dr. Weidong Wang are also acknowledged for their contributions in the bonding process for Type-A2 cells (a manuscript that details MEMS processing [40] is in preparation). Dr. Andres M. Cardenas-Valencia acknowledges the support of the Conacyt and the University of Guadalajara (Mexico) and the University of South Florida, for financial support for his doctoral studies and allowing him to accept a postdoctoral position at the USF-Center for Ocean technology where he is currently employed.

Appendix A. Model to predict the voltage under load of a given cell

The cell potential output under load can be obtained by doing a basic charge (or ion species) balance. If it is assumed that the current density, J is restricted by ion-transport limitations, and can be expressed through the diffusivity, D, and the concentration of ions C, then

$$J = D\frac{\mathrm{d}C}{\mathrm{d}x} \tag{A.1}$$

To include the electrical load into our calculations, one can write the current, i, in terms of the potential, V, electrode areas, A, and the current density, J, which can be written in terms of the electric field, E, and the conductivity, σ, as

$$i = JA = \sigma EA = \zeta\, \mathrm{e_c} C\mu \left(\frac{\mathrm{d}V}{\mathrm{d}x}\right) A, \tag{A.2}$$

C is the ionic concentration, ζ the ionic valence, $\mathrm{e_c}$ the electron charge, and μ is the ion mobility. This last equality, implies that the model assumes the conductivity in the electrode proximity due exclusively to the characteristic ions of the respective electrodes. Eqs. (A.1) and (A.2) and Ohms' law allow one to write,

$$C = \left(\frac{d}{\zeta\, \mathrm{e}\mu A}\right)\left(\frac{i}{V_{\mathrm{load}}}\right) = \left(\frac{d}{\zeta\, \mathrm{e}\mu A}\right)\left(\frac{1}{R_{\mathrm{load}}}\right) \tag{A.3}$$

Combining Eqs. (A.1)–(A.3), and rearranging one obtains the following expression that relates the cell potential under load, V_{load}, with the open circuit voltage, V_{oc} and the impedance load, R_{load};

$$V_{\mathrm{load}} = \left[V_{\mathrm{oc}} + \left(\frac{D}{\mu}\right) \ln\left(\frac{d}{\zeta\, \mathrm{e}\mu A}\right)\right] - \left(\frac{D}{\mu}\right) \ln(R_{\mathrm{load}}) \tag{A.4}$$

Since the cell is comprised of two electrodes, it is expected that two limiting situations occur during operation of the cell. Ion-diffusion to each electrode is expected to control the overall potential, and two linear models, each for a specific current load range, define the cell potential behavior, as shown in the experimental results.

Appendix B. Kinetic modeling

To model the chemical kinetics of ClO^- production of OH^- with H_2O, the mechanism described in Fig. 2(B) was proposed. The assumption of first order in the reactions kinetics, allows one to write the following differential equations system:

$$\begin{aligned}\frac{d([OH^-])}{dt} &= -k_3[OH^-] - k_1[OH^-] + k_2[OCl^-]\\ \frac{d([OH^-])}{dt} &= -k_3[OH^-] - k_2[OCl^-]\\ \frac{d([OH^-])}{dt} &= -k_3[OH^-]\end{aligned} \tag{B.1}$$

Now, to simplify the final expressions the following equalities are defined: $H{\equiv}OH^-$, $Cl{\equiv}OCl^-$, and $H^*{\equiv}OH^{-*}$, and the values a, b and d, as functions of algebraic expressions of the kinetic constants k_1, k_2 and k_3, it can be shown that

$$\frac{C}{C_o} = F\,e^{-at} + G\,e^{-bt}, \quad \text{where } F \equiv \frac{b(a-d)}{d(a-b)} \quad \text{and}$$

$$G \equiv \frac{a(d-b)}{d(a-b)}, \tag{B.2}$$

which implies that $F+G=1$. Eqs. (B.1) and (B.2) are used to obtain the current under load;

$$\frac{i}{i_o} = \left[\frac{(\partial C/\partial t)_t}{(\partial C/\partial t)_{t=0}}\right] = P\,e^{-at} + Q\,e^{-bt},$$

$$\text{where } P \equiv \frac{aF}{aF+bG} \quad \text{and} \quad Q \equiv \frac{bG}{aF+bG} \tag{B.3}$$

References

[1] R.A. Powers, Proc. IEEE 83 (1995) 687–693.
[2] R.J. Brodd, Electrochem. Soc. Interface 8 (1999) 20–23.
[3] D. Linden, T.B. Reddy, Handbook of Batteries, third ed., McGraw-Hill Handbooks, New York, 2002.
[4] S. Samson, L. Langebrake, C. Lembke, J. Patten, OCEANS '99 MTS/IEEE, vol. 1, 1999, pp. 58–63.
[5] L. Langebrake, C. Lembke, R.H. Weisberg, R.H. Byrne, D.R. Russell, G. Tilbury, R. Carr, Oceans '02 MTS/IEEE, vol. 1, 2002, pp. 98–103.
[6] L.R. Adornato, E.A. Kaltenbacher, T.A. Villareal, R.H. Byrne, Deep Sea Res. Part I: Ocean. Res. Papers 52 (2005) 543–551.
[7] A.M. Bradley, M.D. Feezor, H. Singh, F. Yates Sorrell, J. Oceanic Eng. IEEE 26 (2001) 526–538.
[8] L. Langebrake, S. Samson, K.A. Kaltenbacher, E.T. Steimle, J.T. Patten, C.E. Lembke, R.H. Byrne, K. Carder, Oceans 2000 MTS/IEEE Conference and Exhibition, vol. 1, 2000, pp. 617–621.
[9] G.P.G. Kibelka, T. Short, R. Toler, K. Strawn, J.E. Edkins, R.H. Byrne, Talanta 64 (2004) 961–969.
[10] L.R. Adornato, E.A. Kaltenbacher, T.A. Villareal, R.H. Byrne, Seas II uses now metal hydride batteries, May 2006, Unpublished data.
[11] M. Kontitsis, R.D. Garcia, K.P. Valavanis, J. Intell. Rob. Syst. 44 (2005) 139–159.
[12] G.J. May, J. Power Sources 58 (2006) 1117–1123.
[13] C. Vincent, IEE Rev. 45 (1999) 65–68.
[14] H. Tsukamoto, IEEE 18 (2003) 21–23.
[15] J.P. Zheng, P.L. Moss, R. Fu, Z. Ma, Y. Xin, G. Au, E.J. Plichta, J. Power Sources 146 (2005) 753–757.
[16] M. Madou, Fundamentals of Microfabrication, CRC Press LLC, 1997.
[17] J.S. Wainright, R.F. Savinell, C.C. Liu, M. Litt, Electrochim. Acta 48 (2003) 2869–2877.
[18] T.J. Yen, N. Fang, X. Zhang, Appl. Phys. Lett. 83 (2003) 4056–4058.
[19] R. Hahn, S. Wagner, A. Schmitz, H. Reichl, J. Power Sources 131 (2004) 73–78.
[20] J. Yeom, R.S. Jayashree, C. Rastogi, M.A. Shannon, P.J.A. Kenis, J. Power Sources 160 (2006) 1058–1064.
[21] J.N. Harb, R.M. LaFollette, R.H. Selfridge, L.L. Howell, J. Power Sources 104 (2002) 46–51.
[22] V.R. Challa, A.M. Cardenas-Valencia, D. Fries, L. Langebrake, R.F. Benson, S. Bhansali, Proc. 16th European Conference on Solid-State Transducers, Prague, Czech Republic, 2002.
[23] A.M. Cardenas-Valencia, D.P. Fries, G. Steimle, H. Broadbent, L.C. Langebrake, R.F. Benson, Proc of the First Intl. Conf. on Fuel Cells, NY, April, 2003.
[24] K.B. Lee, L. Lin, J. Microelectromech. Syst. 12 (2003) 840–847.
[25] A.M. Cardenas-Valencia, V.R. Challa, D. Fries, L. Langebrake, R.F. Benson, S. Bhansali, Sens. Actuators B Chem. 95 (2003) 406–413.
[26] A.M. Cardenas-Valencia, D. Fries, H. Broadbent, L. Langebrake, R.F. Benson, Proc. of the Seventh International Conference on Miniaturized Chemical and BioChemical Analysis Systems, μTAS, 2003, pp. 311–314.
[27] K.B. Lee, J. Micromech. Microeng. 15 (9) (2005) S210–S214.
[28] L. Fu, J.K. Kuo, J.E. Huber, T.J. Lu, J. Phys. 34 (2006) 800–805.
[29] A.M. Cardenas-Valencia, J. Dlutowski, J. Bumgarnen, L. Langebrake, W. Moreno, J. Micromech. Microeng. 16 (2006) 1511–1518.
[30] S. Licht, Col. Surf. A 134 (1) (1998) 241–248.
[31] Q. Li, N.J. Bjerrum, J. Power Sources 110 (2002) 1–10.
[32] D.J. Brodrecht, J.J. Rusek, Appl. Energy 74 (2003) 113–124.
[33] R.F. Benson, A.M. Cardenas-Valencia, L. Langebrake, Aluminum Galvanic Cell, Patent Pending, University of South Florida, USF, Serial No. 10/709,173.
[34] X. Zhang, S.H. Yang, H. Knicle, J. Power Sources 128 (2004) 331–342.
[35] A. Brenner, J. Electrochem. Soc. 143 (1996) 3133–3138.
[36] M.G. Medeiros, E.G. Dow, J. Power Sources 80 (1999) 78–82.
[37] M.G. Medeiros, C.G. Zoski, J. Phys. Chem. B 102 (1998) 9908–9914.
[38] A. Aesar, A Johnson Matthey Company, 26 Parkridge Road, Ward Hill, MA 0183e5-6904, Product Catalogue 2006–2007.
[39] www.cyclotene.com.
[40] J. Dlutowski, C.J. Biver, W. Wang, S. Knighton, J. Bumgarner, L. Langebrake, W. Moreno, A.M. Cardenas-Valencia, Development of BCB-sealed galvanic cells, case study: Al-NaOCl reserve cells, in preparation.
[41] A.M. Cardenas-Valencia, J. Dlutowski, S. Knighton, C.J. Biver, J. Bumgarner, L. Langebrake, Sens. Actuators: Chem. B, in press. (Available online 25 July 2006).
[42] G.E. Cullen, R.S. Hubbard, J. Biol. Chem. 37 (1919) 511–517.
[43] A.M. Cardenas-Valencia, J. Dlutowski, J. Bumgarner, C. Munoz, W. Wang, R. Popuri, L. Langebrake, Sens. Actuators: Phys. A, in press (Available online 22 December 2006).